Structure and corrosion behaviour of Cr$_x$Al(Si)$_y$C coatings fabricated by the vacuum arc discharge technique

A. P. Rubshtein[†], A. B. Vladimirov, S. A. Plotnikov, V. B. Vykhodets, T. E. Kurennykh

[†]rubshtein@imp.uran.ru

M. N. Miheev Institute of Metal Physics of UB of RAS, Ekaterinburg, 620290, Russia

The composition, structure and corrosion behaviour of Cr$_x$Al$_y$(Si)C coatings fabricated by the arc discharge techniques using Cr-Al-Si and graphite cathodes were studied. X-ray photoelectron spectroscopy, X-ray energy-dispersive spectroscopy, nuclear reactions, and Rutherford backscattering methods were applied to determine composition of the coating, X-ray diffraction and transmission electron microscopy — to investigate the structure of the coating. Corrosion tests were performed in an electrochemical cell in a 3.5 % NaCl solution. Depletion of the cathode surface of chromium, screening of Cr$^+$ by C$^+$ in plasma, and selective etching of the coating upper layers are accompanied by a decrease of Cr/(Al + Si) ratio in the coatings compared to the cathode. The carbon content (C_C) in Cr$_x$Al(Si)$_y$C, determined by XPS, EDS and NR, differs by several times. The C_C measured by NR correlates with the results of Raman spectroscopy and confirms the existence of a continuous carbon matrix in Cr$_x$Al$_y$(Si)C. Cr is chemical bonded with carbon, silicon — with carbon and aluminum. The Al-Si system provides the structure feature of Cr$_x$Al(Si)$_y$C: a network of aluminum intersects the amorphous matrix. The mechanical mismatch and weak bond between the Al structures and the amorphous matrix may be the reason for the formation of defects in the form of cracks and microchannels along the boundaries.

Keywords: multicomponent coating, arc discharge technique, composition, structure, corrosion.

1. Introduction

Alloying of carbon coatings with other elements is one of the ways to improve their mechanical and tribological characteristics, corrosion and thermal resistance. Ultrafine carbide inclusions are formed in the carbon matrix owing to alloying with carbide-forming metals (Ti, Mo, W). Carbide inclusions significantly increase the coating hardness [1–3]. Weak carbide forming metals (Cr, Mn, Fe, Co, Ni) usually form completely amorphous or mainly amorphous films with nanocrystallites difficult to identify [4]. Hard and brittle carbide inclusions reduce the ductility and toughness of the coating. In contrast, the alloying using the metals not forming strong bonds with the carbon matrix (Cu, Al) leads to the formation of metal phases [5–6]. Metal phases improve the viscosity, but reduce the hardness. Synthesis of multicomponent coatings, including metal atoms that form strong bonds with carbon, metal atoms that do not form strong bonds with carbon, and non-metal atoms allows to significantly improving the functional characteristics of coatings [6–8]. W. Dai at al [6] establish that the carbide former Cr preferred to form hard carbide components, which increase the hardness; the weak carbide former Al dissolved in the carbon matrix influencing the stresses; Si improves the thermal stability of diamond-like carbon coatings with Al, Cr and Si multi-alloying. A significant change in the structure and properties owing to alloying with Al, Si, Cu, Zr occurs in nitride coatings also [7–9]. The relationship among the hardness, plastic deformation resistance, toughness, tribological properties and Si content was discovered for the nitride CrTiAlSiN [7]. The best physical and mechanical characteristics were achieved at a silicon concentration of 7–9 at.% in TiN/α-Si$_3$N$_4$. Nitride nanocomposite coatings consist of metal nitride nanocrystals less than 5 nm in size, surrounded by an amorphous Si$_3$N$_4$ compounds [10].

Aluminum containing coatings (in particular, Cr$_2$AlC) are prospective as an anti-corrosion owing the formation of protective layers of Al$_2$O$_3$ at elevated temperatures. As the aluminum concentration increases, the coating becomes amorphous with disordered inclusions of nanocrystals 5–15 nm in size [11–12]. This structure provides high hardness, wear- and corrosion resistance. Alloying of Cr$_x$Al$_y$C with silicon enhances their crystallinity making the coating harder with a low friction coefficient and high resistance to plastic deformation [13–14]. Silicon carbide and metal-like silicide, the synthesis of which is very feasible under the deposition conditions of Cr$_x$Al(Si)$_y$C, are chemically inert and resistant to oxygen even at high temperatures. These phases should increase the corrosion resistance of the coating. However, the effect of silicon on the corrosion resistance of Cr$_x$Al$_y$C fabricated by physical vapor deposition (PVD) technique is not available in the literature. Therefore, it is of significance to analyze the corrosion behaviour of silicon doped Cr$_x$Al(Si)$_y$C coatings.

In this study we focus on the composition, structure and corrosion behaviour of Cr$_x$Al(Si)$_y$C fabricated by arc discharge technique. A detailed study of the composition and structure allowed establishing the reason for the deterioration in corrosion resistance of Cr$_x$Al$_y$C coatings alloyed with silicon.

2. Materials and methods

Coatings with a thickness of 3800 nm were deposited using a UVNIPA-001 machine. Before the coating deposition, the substrates were subjected to ion (Ar^+) etching. An arc plasma source with the Cr-Al-Si cathode and pulsed arc plasma source with a graphite cathode were used to deposit the $Cr_xAl(Si)_yC$ coatings. The arc current was 55 A, while the pulse frequency was 15 Hz. Only an arc plasma source with the Cr-Al-Si cathode was used to deposit $Cr_xAl(Si)_y$ coating. The Cr-Al-Si cathode obtained by hot pressing of powders had a uniform structure consisting of an aluminum matrix with inclusions of chromium and silicon [15].

The $Cr_xAl(Si)_yC$ were characterized via X-ray photoelectron spectroscopy (XPS, PHI5702) to obtain the atomic ratio information and bonding structure. The atomic ratio of Cr, Al, Si and C was also characterized by X-ray energy dispersion spectroscopy (EDS, QUANTA 200 microscope equipped with an EDAX analyzer), nuclear reactions (NR) and Rutherford backscattering (RBS) realized on the electrostatic accelerator EG-2M. Only the total concentration of aluminum and silicon (Al+Si) was determined using RBS due to overlapping spectra.

A glancing incidence X-ray diffraction (XRD, Empyrean, PANalytical B.V., PHILIPS) was carried out in the conventional θ/2θ mode using Cu-K$_a$ radiation to analyses the coating phase composition. The glancing incident angle of X-ray was 1°. Transmission electron microscopy (TEM, JEM-200) was used for observation of the coating structures.

Open-circuit potential (OCP) and potentiodynamic polarization tests using an electrochemical workstation were carried out to evaluate the corrosion resistances of $Cr_xAl(Si)_yC$ in a 3.5 wt.% NaCl solution at room temperature. An Ag/AgCl electrode serve as reference. The potentiodynamic polarization tests were carried out at a scan rate of 2 mV·s^{-1}.

3. Results and discussion

The compositions of Cr_xAl_ySi and $Cr_xAl(Si)_yC$ coatings, as well as the as received Cr-Al-Si cathode (cathode 1) and used cathode (cathode 2) are presented in Table 1. The carbon content (C_C) in $Cr_xAl(Si)_yC$, determined by XPS, EDS and NR, differs by several times. The highest carbon content is determined by XPS. There are two reasons for that: contamination of the coating surface with hydrocarbons [16] and a small depth of analysis (several monolayers). That is why XPS does not provide reliable information on the average atomic ratio over the coating thickness. According to the EDS, the C_C is 4 times lower compared to the XPS, and is 18 at.%. This content does not sufficient for the formation of an amorphous matrix in the coating, existing of which was previously establish by Raman spectroscopy [13]. The C_C, measured by nuclear reactions, 42.3 at.%, correlates with the results of Raman spectroscopy and confirms the formation of carbon amorphous matrix in the form of a continuous cluster. In addition, oxygen was detected at a level of several at.% in coatings, owing to the oxygen presence in cathodes and residual atmosphere in the working chamber.

The carbon content C_C obtained with XPS, EDS and RBS affect the values of C_{Cr}, C_{Al} and C_{Si}. Therefore, using of the ratio Cr/(Al+Si) is more correct. According to EDS and RBS results, the Cr/(Al+Si) ratio in $Cr_xAl(Si)_yC$ is lower than in cathod1 and cathode 2 (Table 1). The depletion of the cathode surface with chromium under arc action leads to a gradient of its concentration over the coating thickness. However, according to EDS, Cr/(Al+Si) in $Cr_xAl(Si)_yC$ is lower than in $Cr_xAl(Si)_y$. The Al atoms act as obstructers hindering the binding of Cr atoms with C atoms [17]. Moreover screening of Cr^+ with C^+ occurring in plasma reduces the chromium content in $Cr_xAl(Si)_yC$. Early it was reported, that an increasing C^+ in plasma is accompanied by a decrease in Cr in

Table 1. Composition of cathodes and coatings determined by various techniques.

Test method	Cathode 1	Cathode 2	Cr_xAl_ySi	$Cr_xAl(Si)_yC$
	Content, at.%			
C_C				
XPS	-	-	-	72.1
EDX	-	-	-	18.6
NR	-	-	-	42.3
C_{Cr}				
XPS	-	-	-	0.9
EDX	34.2	29.1	26.7	20.4
RBS	-	-	-	11.0
C_{Al}				
XPS	-	-	-	13.0
EDX	53.9	59.8	60.8	51.6
C_{Si}				
XPS			-	13.4
EDX	7.5	7.5	8.1	8.1
C_O				
EDX	4.4	3.6	4.4	1.3
NR	-	-	-	2.8
Cr/(Al+Si) ratio				
XPS	-	-	-	0.03
EDX	0.56	0.45	0.43	0.34
RBS	-	-	-	0.25

Cr_xAl_yC [18]. The $Cr_xAl(Si)_y$ was deposited with the switched off pulsed arc source with a graphite cathode. In this case, the working plasma does not contain carbon ions. Another reason for the difference in the atomic ratio in the coating and cathode may be the selective sputtering of the upper layers of the coating under action of accelerated ions. Thus, the atomic ratio in the coating depends not only on the atomic ratio in the cathode but also on the processes occurring on the cathode surface, in the plasma, and in the upper layers of the coating.

The very small value of Cr/(Al+Si) in $Cr_xAl(Si)_yC$, determined by XPS, attracts attention. An anomalously low content of Cr in hydrogen-containing carbon films doped with copper and chromium was detected with XPS by Jia et all [19]. At a ratio of Cr/Cu in the target of 1.5, Cr/Cu in the Cr_xCu_yC films was less than 0.08. The authors suggested that hydrocarbon ions could react with Cr on the target surface, forming Cr_xC_y carbides, which prevent Cr sputtering. However, we did not find a significant carbon content in the cathode 2. This means, that the formation of Cr_xC_y on the cathode surface does not occur in our experiment. We assume that during ion cleaning of the coating surface in an XPS analyzer, chipping of carbide particles is possible. In this case, the C_{Cr} decreases at a depth of several monolayers.

XPS is one of the most promising investigation techniques due to its ability to give information about the chemical bonds in materials. The survey X-ray photoelectron spectrum (XPS) of $Cr_xAl(Si)_yC$ con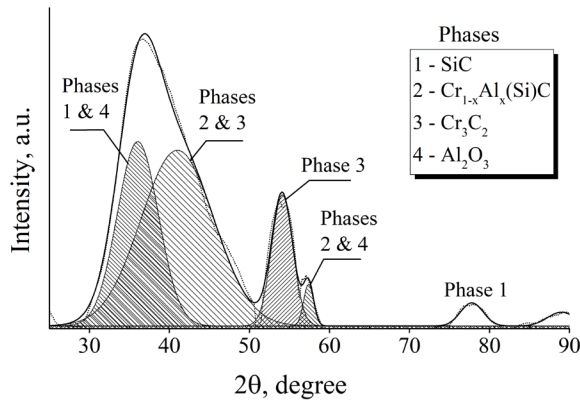tains five major spectral lines from the core levels of C1s, O1s, Cr2p, Al2p, and Si2p (Fig. 1a). The O1s spectrum is located in the region from 532.1 to 532.3 eV, which is typical for adsorbed oxygen.

Two peaks at ≈577.2 and 580.1 eV deconvoluted from the major Cr2p peak could be assigned to Cr-O bonds in Cr_2O_3 and CrO_2 (Fig. 1b). A small peak at $E=574.3$ eV can be attributed to metallic chromium and chromium compounds with carbon. The Cr2p peak have not to be used effectively to differentiate the chemical bonds of metallic Cr and Cr-C. However, the content of metallic Cr can be reflected indirectly by the content of Cr_2O_3, because the reactivity of metallic Cr with O to form Cr_2O_3 was higher than that of Cr-C [20 – 21]. The XPS Al2p spectrum (Fig. 1c) after deconvolution includes three peaks. The most intense peak in the energy range $E=73.9 – 74.1$ eV is characteristic of Al-Si bonds. Other two small peaks correspond to metallic aluminum ($E=72.8$ eV) and aluminum oxide ($E=75.6$ eV). The XPS Si2p spectrum after deconvolution contains a pronounced peak in the energy range $E=102.1 – 102.2$ eV corresponding to Si-Al bonds (Fig. 1d). Less intense peaks are located in the energy ranges $E=101.2 – 101.3$ and $E=103.1 – 103.4$ eV corresponding to silicon carbides and oxides [22]. The presence of oxide phases of Cr, Al and Si is the result of oxidation of the surface layer.

An XRD analysis was performed to identify the phases in $Cr_xAl(Si)_yC$. The diffuse diffraction peaks in the XRD spectrum (Fig. 2) indicate the low crystallization and amorphous component. The fused peak centers were obtained by fitting the XRD spectrum. The main phases, the growth of
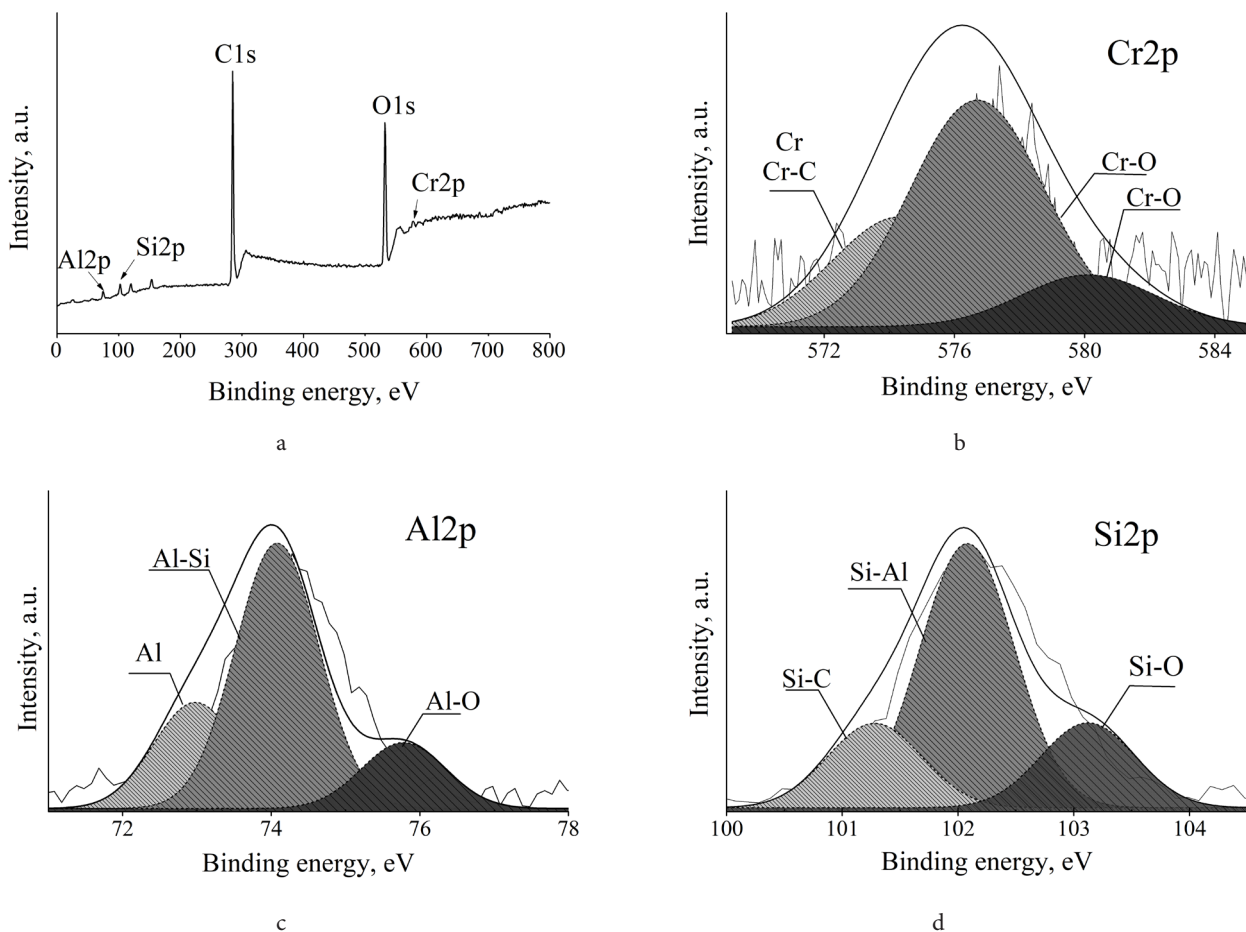
Fig. 1. The survey XPS spectrum for $Cr_xAl(Si)_yC$ (a); XPS Cr2p spectrum (b), XPS Al2p spectrum (c) and Si2p spectrum (d) for $Cr_xAl(Si)_yC$.

Fig. 2. XRD spectrum for $Cr_xAl(Si)_yC$.

Fig. 3. TEM images of $Cr_xAl(Si)_yC$. Bright-field image with microdiffraction pattern (upper left corner), rings marked with numbers, dendritic structures marked with a dashed circle (a); dark-field image (b).

which in $Cr_xAl(Si)_yC$ according to XPS is most probable, are chromium and silicon carbides, aluminum oxide, and metal aluminosilicide (Fig. 2). It is difficult to determine accurately the phases and their ratio using this X-ray spectrum. The formation in coating of Al amorphous phase and a solid solution with silicon is also feasible. The existence of metallic aluminum and Al-Si bonds in $Cr_xAl(Si)_yC$ is confirmed with XPS.

The Al amorphous phase and a solid solution with silicon are characteristics of Al-Si metastable eutectic system. According to the phase diagram, there are three phases in the Al-Si system: a liquid unlimited solution of aluminum and silicon atoms (L), a solid solution of silicon in aluminum (α), and a solid solution of aluminum in silicon (β). Crystallization with the precipitation of α and β phases begins at a temperature below 577°C [23]. The melting and crystallization of the Al-Si eutectic is feasible inside the local areas of $Cr_xAl(Si)_yC$. In the technological conditions for the deposition of $Cr_xAl(Si)_yC$ could be realized the subplantation growth mechanism [24 – 25]. Accelerated ions, passing through the upper unconsolidated layers, penetrate inside the bulk of coating. The stopping and trapping of the bombarding ions and the material modifications involve three different stages: ions stopping via (atomic) collisions, ionization and phonon excitations (the "collisional stage"); dissipation of the excess energy in the target (the conduct "thermalization stage"); the long-term relaxation stage where diffusion, chemical reactions and phase transformations take place [24]. In the third stage, melting of the eutectic occurs in the local areas. The temperature of the entire coating does not rise above 300°C, because the complete graphitization of the carbon cluster is not confirmed by the Raman spectroscopy [13].

The eutectic melt migrates over the coating bulk. A branched network of dendrites, resulting of melt crystallization, crosses the amorphous matrix (Fig. 3a). Dendrite-like structures are weakly bound to the amorphous matrix, since aluminum does not form strong bonds with carbon. Therefore, the boundaries along the crystallized eutectic are feasible to contain microchannels that should negatively affect the corrosion resistance of the coating material. The narrow rings with separate spots and diffuse central spot in the SAED pattern of $Cr_xAl(Si)_yC$ indicate
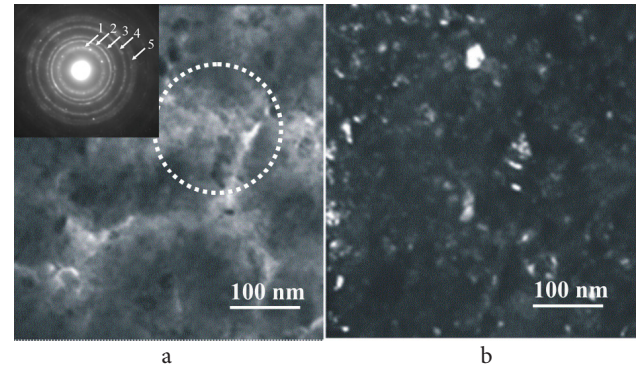
that its structure includes highly dispersed nanocrystalline inclusions. The nanocrystalline inclusions with a size of 10 – 20 nm and conglomerates with a size of up to 30 nm are visible in the dark-field image (Fig. 3b). Inclusions may belong to one of the phases listed in the Table 2.

The results of the corrosion test of $Cr_xAl(Si)_yC$ are shown in Table 3. The open circuit potential (OCP) of $Cr_xAl(Si)_yC$ is higher than that of Cr_xAl_yC. That means $Cr_xAl(Si)_yC$ is better corrosion resistant material. Silicon carbide and metal-like silicide detected with XPS and XRD in $Cr_xAl(Si)_yC$ are chemically inert and resistant to oxygen even at high temperatures. However, a lower E_{corr} and a significantly higher value of I_{corr} determined in potentiodynamic polarization tests, indicate a deterioration in corrosion resistance of $Cr_xAl(Si)_yC$ compared to Cr_xAl_yC. Although the corrosion current density of $Cr_xAl(Si)_yC$ is higher than that of Cr_xAl_yC, it is still lower than that of stainless steel. The Al-Si eutectic system in the $Cr_xAl(Si)_yC$ is a result of silicon alloying of the Cr_xAl_yC. The Al-Si eutectic provides the structure feature of the $Cr_xAl(Si)_yC$: network of crystallized aluminum crosses the amorphous matrix. The mechanical mismatch and weak bond between the crystallized aluminum and the amorphous matrix provides boundaries with the defects. Defects reduce the protective properties of $Cr_xAl(Si)_yC$ coatings.

Table 2. Estimated phases after unscramble SAED.

No ring	Phases
1	Graphite
2	SiC, Cr_3C_2, Al_2O_3
3	$Cr_2Al(Si)C$, SiC, Cr_3C_2, Al_2O_3
4	$Cr_2Al(Si)C$, Cr_3C_2, Al_2O_3
5	SiC, Al_2O_3

Table 3. Electrochemical data for the steel and the coatings in the 3.5 wt.% NaCl solution.

	Stainless steel	Cr_xAl_yC [12]	$Cr_xAl(Si)_yC$
OCP(V)	−0.435	−0.015	0.037
E_{corr} (V)	−0.452	−0.223	−0.248
I_{corr} (nAcm^{-2})	19700	61.51	3170.2

4. Conclusions

The atomic ratio of Cr, Al, and Si in $Cr_xAl(Si)_yC$ deposited by an arc discharge differs from the atomic ratio of these elements in the cathode. Depletion of the cathode surface layer of chromium, screening of chromium ions by carbon ions in plasma, and selective etching of the coating upper layers leads to a decrease Cr/(Al+Si) ratio in the coating compared to the cathode. The carbon content in $Cr_xAl(Si)_yC$, determined by XPS, EDS, and NR, differed by several times. The C_C measured by NR correlates with the results of Raman spectroscopy and confirms the existence of a continuous carbon matrix in $Cr_xAl_y(Si)C$.

According to XPS spectra, Cr is chemical bonded with carbon, silicon — with carbon and aluminum. The results of X-ray diffraction and transmission electron microscopy study confirmed the formation of carbides and metal aluminosilicide. The structure of $Cr_xAl(Si)_yC$ is amorphous-nanocrystalline. Amorphous matrix with nanocrystalline carbides inclusions contain a network of aluminum dendrite like precipitation. Dendrite like precipitation is the result of addition silicon to Cr-Al-Si target. Silicon binds of aluminum into the liquid phase of Al-Si system. Coating growth by the "subplantation" mechanism with temperature spikes in local areas creates favorable conditions for the melting and crystallization of the Al-Si eutectic. The mechanical mismatch and weak bond between the dendritic structures and the amorphous matrix may be the reason for the creation of the defects around boundaries. Defects reduce the protective properties of the coating.

References

1. X. C. Tang, H. J. Wang, L. Feng, L. X. Shao, C. W. Zou. Appl. Surf. Sci. 311, 758 (2014). Crossref
2. L. Cao, J. Liu, Y. Wan, J. Pu. Diam. Relat. Mater. 109, 108019 (2020). Crossref
3. V. S. Dhandapani, R. Subbiah, E. Thangavel, M. Arumugam, K. Park, Z. M. Gasem, V. Veeraragavan, D.-E. Kim. Appl. Surf. Sci. 371, 262 (2016). Crossref
4. U. Jansson, E. Lewin. Thin Solid Films. 536, 1 (2013). Crossref
5. W. Dai, A. Wang, Q. Wang. Surf. Coat. Technol. 272, 33 (2015). Crossref
6. W. Dai, X. Gao, J. Liu, Q. Wang. Diam. Relat. Mater. 70, 98 (2016). Crossref
7. Y.-C. Kuo, C.-J. Wang, J.-W. Lee. Thin Solid Films. 638, 220 (2017). Crossref
8. C. Tritremmel, R. Daniel, M. Lechthaler, P. Polcik, C. Mitterer. Thin Solid Films. 534, 403 (2013). Crossref
9. J. L. Endrino, S. Palacin, M. H. Aguirre, A. Gutierrez, F. Schafers. Acta Materialia. 55, 2129 (2007). Crossref
10. S. Veprek, R. F. Zhang, A. S. Argon. Phil. Mag. Lett. 87, 955 (2007). Crossref
11. M. Hopfeld, R. Grieseler, A. Vogel, H. Romanus, P. Schaaf. Surf. Coat. Technol. 257, 286 (2014). Crossref
12. A. P. Rubshtein, K. Gao, A. B. Vladimirov, S. A. Plotnikov, B. Zhang, J. Zhang. Surf. Coat. Technol. 377, 124912 (2019). Crossref
13. A. P. Rubshtein, A. B. Vladimirov, S. A. Plotnikov, E. G. Volkova. J. Surf. Investig.-X-RA. 15, 961 (2021). Crossref
14. A. P. Rubshtein, V. A. Zavalishin, A. B. Vladimirov, S. A. Plotnikov. J. Phys.: Conf. Ser. 1799, 012026 (2021). Crossref
15. G. A. Pribytkov, V. V. Korzhova, A. P. Savitskii. AIP Conf. Proceed. 1623, 511 (2014). Crossref
16. J. B. Reed. Electron Microprobe Analysis and Scanning Electron Microscopy in Geology. Cambridge University Press (2005). Crossref
17. T.-C. Fu, G.-W. Li. Appl. Surf. Sci. 253, 1260 (2006). Crossref
18. A. P. Rubshtein, A. B. Vladimirov, S. A. Plotnikov. Sol. Stat. Phenom. 279, 160 (2018). Crossref
19. Q. Jia, Z. Mu, X. Zhang, B. Zhang, R. Liu, K. Gao, Y. Yu, Z. Lai, J. Zhang. Mater. Today Chem. 21, 100521 (2021). Crossref
20. K. M. Jiang, D. Q. Zhao, X. Jiang, Q. Huang, L. J. Miao, H. M. Lu, Y. Li. J. Alloy Compd. 750, 560 (2018). Crossref
21. K. Nygren, M. Andersson, J. Hogstrom, W. Fredriksson, K. Edstrom, L. Nyholm, U. Jansson. Appl. Surf. Sci. 305, 143 (2014). Crossref
22. A. Tamayo, F. Rubio, M. A. Mazo, J. Rubio. Boletín de la Sociedad Española de Cerámica y Vidrio. 57, 231 (2018). Crossref
23. K. S. Chandra, D. Sarkar. Mater. Chem. Phys. 277, 125493 (2022). Crossref
24. Y. Lifshitz. Diam. Relat. Mater. 8, 1659 (1999). Crossref
25. A. P. Rubshtein, A. B. Vladimirov, S. A. Plotnikov. J. Phys.: Conf. Ser. 1281, 012065 (2019). Crossref